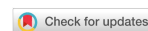


Research Article

Open Access



Sulfur poisoning mechanism of LSCF cathode material in the presence of SO₂: a computational and experimental study

Rui Wang¹ , Lucas R. Parent², Yu Zhong^{1,*}

¹Mechanical and Materials Engineering Department, Worcester Polytechnic Institute, Worcester, MA 01609, USA.

²Innovation Partnership Building, University of Connecticut, Storrs, CT 06269, USA.

*Correspondence to: Prof. Yu Zhong, Mechanical and Materials Engineering Department, Worcester Polytechnic Institute, 100 Institute Road, Worcester, MA 01609, USA. E-mail: yzhong@wpi.edu

How to cite this article: Wang R, Parent LR, Zhong Y. Sulfur poisoning mechanism of LSCF cathode material in the presence of SO₂: a computational and experimental study. *J Mater Inf* 2023;3:3. <https://dx.doi.org/10.20517/jmi.2022.45>

Received: 19 Dec 2022 **First Decision:** 30 Jan 2023 **Revised:** 15 Feb 2023 **Accepted:** 6 Mar 2023 **Published:** 9 Mar 2023

Academic Editors: Qian Li, William Yi Wang **Copy Editor:** Ke-Cui Yang **Production Editor:** Ke-Cui Yang

Abstract

Aiming at the comprehensive understanding of the single sulfur poisoning effect and, eventually, the multiple impurities poisoning phenomena on the SOFC (Solid Oxide Fuel Cell) cathode materials, the sulfur poisoning effect on the (La_{0.6}Sr_{0.4})_{0.95}Co_{0.2}Fe_{0.8}O₃ (LSCF-6428) has been investigated in the presence of 10 ppm SO₂ at 800, 900, and 1,000 °C, respectively, with a combined computational and experimental approach. The good agreement between the CALPHAD (Computer Coupling of Phase Diagrams and Thermochemistry) simulations and the XRD (X-Ray Diffraction), SEM (Scanning Electron Microscopy), and TEM (Transmission Electron Microscopy) characterization results support the reliability of the CALPHAD approach in the SOFC field. Furthermore, comprehensive simulations were made to understand the impact of temperature, P(SO₂), P(O₂), and Sr concentration on the threshold of SrSO₄ stability. Results showed that the formation of SrSO₄ is thermodynamically favored at lower temperatures, higher P(SO₂), higher P(O₂), and higher Sr concentration. Finally, comparisons were also made between LSCF-6428 and LSM20 (La_{0.8}Sr_{0.2}MnO₃) using simulations, which confirmed that LSCF-6428 is a poor sulfur-tolerant cathode, in agreement with the literature.

Keywords: LSCF cathode, CALPHAD, sulfur poisoning, long-term degradation, accelerated testing



© The Author(s) 2023. **Open Access** This article is licensed under a Creative Commons Attribution 4.0 International License (<https://creativecommons.org/licenses/by/4.0/>), which permits unrestricted use, sharing, adaptation, distribution and reproduction in any medium or format, for any purpose, even commercially, as long as you give appropriate credit to the original author(s) and the source, provide a link to the Creative Commons license, and indicate if changes were made.



INTRODUCTION

Mixed Ionic and Electronic Conducting (MIEC) (La, Sr)(Co, Fe)O₃ (LSCF) is one of the most promising Solid Oxide Fuel Cell (SOFC) cathodes due to its comprehensive electrochemical properties. It has been widely applied at intermediate conditions in the energy conversion from fossil fuels to electricity to tackle the penalty of CO₂ emission and poor efficiency from traditional oxy-fuel combustion^[1,2]. However, SOFC cathode materials suffer from thermodynamic instability in their long-term durability in the presence of several impurities, of which SO₂ is known to be a concern^[3,4]. Thus, developing a comprehensive understanding of the sulfur poisoning of LSCF cathodes in the presence of SO₂ impurity is necessary to address the long-term degradation of the SOFC cathode systems at operating conditions.

It is reported that a trace amount of SO₂ in air, as low as in part per million (ppm) level, can still cause a performance drop and shorten the service life of LSCF cathodes due to the formation of the detrimental secondary phases^[5]. Liu *et al.*^[6] first reported the sulfur poisoning of an LSCF cathode in the presence of 1 and 20 ppm of SO₂ at 800 °C for 1,000 h. Results suggested that the LSCF has a low tolerance to sulfur poisoning even with 1 ppm SO₂. Moreover, the degradation rate of LSCF was 8 times higher than that of LSM at 20 ppm SO₂ because of the formation of SrSO₄ in LSCF. In the same year, Wang *et al.*^[7] reported the formation of SrSO₄, La₂O₂SO₄, and CoFe₂O₄ in 100 ppm SO₂ at 800 °C for 24 h, SrSO₄ and CoFe₂O₄ in 10 and 1 ppm SO₂ at 800 °C for 24 h, respectively. The cell was free from sulfur poisoning in 0.1 ppm SO₂ for 24 h and SO₂-free air for 100 h at 800 °C, respectively, indicating a thermodynamic threshold or a diffusion-controlled mechanism for the sulfur poisoning process. Wang *et al.*^[8] reported the formation of SrSO₄ in the presence of 20mg/L SO₂ at 800 °C for 500 h and concluded that LSCF exhibited poorer durability than LSM against SO₂ poisoning. Later, Wang *et al.*^[9] investigated the effect of Sr concentration on the sulfur poisoning of LSCF cathodes, namely (La_{0.6}Sr_{0.4})(Co_{0.2}Fe_{0.8})O₃ (LSCF-6428) and (La_{0.8}Sr_{0.2})(Co_{0.2}Fe_{0.8})O₃ (LSCF-8228), at 800 °C with 1 ppm SO₂. They concluded that the sulfur poisoning is much more severe for the less active LSCF-8228 cathode, even though the volume of SrSO₄ formed is much larger in LSCF-6428 due to it having more available electrochemically active sites. Moreover, Wang *et al.*^[10] evaluated the SO₂ poisoning phenomena of LSCF-6428 cathodes with 0.1 ppm SO₂-air at 800 °C for 100 h by varying the flow rate (25, 50, and 90 mL min⁻¹). They concluded that SrSO₄ formed on the surface of the LSCF-6428 first due to the fast absorption of the SO₂ and then concentrated in the vicinity of the triple phase boundaries (TPBs) under a polarization condition. Subsequently, Wang and Jiang^[11] reviewed the mechanism of SO₂ poisoning on both LSCF and LSM cathodes. They reported that the sulfur poisoning effect was more pronounced at lower temperatures for both LSCF and LSM cathodes. More importantly, it was most pronounced on the surface of the LSCF cathode and more evident on the interface of LSM/YSZ TPBs. Wang *et al.*^[12] investigated the interrelation between sulfur poisoning and performance degradation of LSCF in the presence of 1 ppm SO₂ at 700 °C, 750 °C, and 800 °C, respectively. They found that the performance degradation was more severe at either 700 °C or 750 °C, even though no significant sulfur was detected in either of these two samples.

Up to now, there are two principal methods to investigate the relationship between the stabilities of the electrodes and the long-term degradation under SOFC applications, CALPHAD^[13-17] and DFT (Density-Functional Theory)^[18,19]. Both can provide a potential approach to designing highly efficient and stable electrode materials with excellent impurity tolerance for SOFCs. Darvish *et al.*^[15] reported the impacts of temperatures, SO₂ partial pressure (P(SO₂)), oxygen partial pressure (P(O₂)), and Sr content on the sulfur poisoning phenomena of the LSCF cathode using the CALPHAD approach and electrochemical analysis. They concluded that the formation of SrSO₄ and spinel phase is thermodynamically in favor of higher P(SO₂), higher P(O₂), lower temperatures, and higher Sr content. Later, Wang *et al.*^[5] reviewed the sulfur poisoning of SOFCs, especially the LSCF cathode, using a very detailed literature review with a corresponding chemical reaction sequence taking into account the parameters like P(SO₂), temperature,

P(O₂), and Sr content. The primary poisoning mechanism proposed was the formation of SrSO₄ from the reaction of SO₂ with SrO and O₂ to form SrSO₄. Subsequent reactions would start to form other sulfur-containing phases like La₂O₂SO₄ and La₂(SO₄)₃ through a reaction with the La components. However, much remains unknown as to how these poisoning reactions are affected by the structure and composition of the cathode material, which limits our ability to design cathodes with improved long-term stability in the presence of natural SO₂ impurities. Moreover, a comprehensive understanding of the relationship between the long-term degradation and single or eventually multiple gas impurities poisoning effects is still needed.

In this work, we have utilized a combined computational and experimental approach to understand the sulfur poisoning mechanism(s) and improve the long-term durability of LSCF cathodes in order to develop better-performing sulfur-tolerant cathode materials in the future. We first examined the agreement between the simulation approach and the experimental observations at various conditions, confirming the reliability of CALPHAD for poisoning simulations in these cathode systems. Using this approach, we then investigated the accelerated testing protocol, which has become the standard method for conducting sulfur poisoning experiments involving LSCF cathode materials. We found that our simulation approach is able to predict in which systems (cathode material and treatment environment) the accelerated testing protocols reflect actual operating conditions. Finally, in-depth simulations were done for LSCF and compared with those for LSM to help understand the LSCF cell system and suggest directions toward alternative cathode materials that have superior sulfur tolerance.

EXPERIMENTAL PROCEDURE

The as-received (La_{0.6}Sr_{0.4})_{0.95}Co_{0.2}Fe_{0.8}O₃ (denoted as LSCF-6428) powders (FuelCellMaterials) were shaped into several pellets with thickness and diameter of around 1 and 13 mm, respectively. Afterward, the pellets were pre-sintered in the ambient air at 1,200 °C for 2h to facilitate handling and remove the binders. Later, the pre-sintered pellets were heat-treated at 800 °C, 900 °C, and 1,000 °C under SO₂-containing dry air (10ppm SO₂ balanced with dry air, Airgas) or dry Argon (10ppm SO₂ balanced with Argon, Airgas) in the tube furnace (OTF-1500X-III, MTI Corporation) for 2 days. The furnace was equipped with 3 independent temperature zones, which allowed the above experiments with the same atmospheric but different temperature conditions to be run in the same batch. Finally, the samples were collected after furnace cooling for further characterization.

The crystal structures of all the samples, including the commercial powder, pre-sintered and heat-treated pellets, were examined by X-ray Diffraction with a Cu tube (PANalytical EMPYREAN) in the range of 20-60°. Later, the microstructure and elemental distributions of the heat-treated pellets were investigated by Scanning Electron Microscopy (SEM) (JEOL JSM-7000F) coupled with Energy-dispersive X-ray Spectroscopy (EDS) (Oxford Instrument X-MAX^N) to characterize the secondary phases. Transmission electron microscope (TEM) samples, ca. 100 nm thick cross-sections mounted on Cu support grids, were prepared using a Thermo Fisher Helios 460F1 dual-beam focused ion beam (FIB-SEM) using a Ga ion beam and standard FIB lift-out procedures to minimize ion damage/implantation. The electron beam was used to deposit a carbon protective layer on the top surface of each lift-out lamella, and the voltage of the cutting ion beam was progressively lowered as each lift-out lamella was thinned down to ca. 100 nm and cleaned. Each FIB-prepared TEM sample was characterized by TEM imaging, diffraction, and spectroscopy (elemental mapping).

Bright Field TEM images and diffraction patterns were obtained for each FIB-prepared TEM sample using a Thermo Fisher Talos TEM equipped with a CETA-M camera, operating at 200 keV, gun lens = 4, spot size = 8, CLA(2) = 70 μm, and beam current: ca. 0.3 nA. An objective lens aperture (OLA) of 70 μm was

used for imaging, and a selected area diffraction (SAD) aperture of 40 μm was used for diffraction; in diffraction mode, the camera length was 1.1 m TEM images and diffraction patterns were acquired and analyzed using Thermo Fisher TIA software.

Scanning-TEM (STEM) images and STEM-EDS elemental maps were obtained for each FIB-prepared TEM sample using a Thermo Fisher Titan Themis TEM operating at 300 keV, gun lens = 3, spot size = 3, CLA(2) = 70 μm , camera length = 130 mm, and beam current: ca. 1.0 nA, and equipped with a Thermo Fisher Super-X Si drift detector (SSD) x-ray spectrometer (ca. 25-35 kcps during STEM-EDS map acquisition on the sample). STEM-EDS spectra and elemental maps were acquired and analyzed using Thermo Fisher Velox software, with input parameters set as: sample thickness: 100 nm, density correction: 6.0 g/cm^3 , Brown-Powell Ionization cross-section model, 1 sigma Gaussian blur for pre-filter and for post-filter.

COMPUTATIONAL PROCEDURE

The CALPHAD approach is considered the computational tool in the present study, which is highly dependent on the reliability of the thermodynamic databases that are usually assessed and constructed using existing literature data. With the corresponding database ready, thermodynamic simulations can thus be conducted using the minimization of the Gibbs free energy of the current system in the Thermo-Calc software. So far, the CALPHAD approach has already been considered and utilized extensively and proven to be a significantly effective tool in the field of SOFCs^[13-16,20-24].

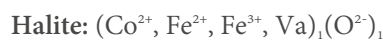
To perform the simulations in the current LSCF system, the thermodynamic database established by Zhang^[25] has been employed in the present work, where detailed thermodynamic parameters can be found. Based on the compound energy formalism, the LSCF perovskite phase is modeled with three sublattices:



where Va stands for Vacancy. There are, in total, 42 end-members in this perovskite phase, such as $(\text{La}^{3+})_1$, $(\text{Fe}^{3+})_1(\text{O}^{2-})_3$, where most of them are not charge neutral. The charge neutrality will be considered and maintained when doing simulations in Thermo-calc. Thus, the Gibbs energy per mole molecule can be described via the CALPHAD formalism:

$$G_m = \sum_{i,j,k} y_i y_j y_k {}^\circ G_{i:j:k}^{Prv} + RT \left(\sum y_i \ln y_i + \sum y_j \ln y_j + 3 \sum y_k \ln y_k \right) + {}^{Ex} G_m^{Prv}$$

where y_i , y_j , and y_k represent the site fraction of each species in A-, B-, and oxygen-site, respectively. ${}^\circ G_{i:j:k}^{Prv}$ is the molar Gibbs energy of the end-members in the system, while ${}^{Ex} G_m^{Prv}$ is the excess Gibbs energy taking into account the interaction parameters among the sublattices. Meanwhile, several oxide solution phases are predicted to form during the simulations, of which the Co/Fe-containing Halite and Spinel phases, as the most important secondary phases, are described as:



Similar to the treatment in our previous works^[15,17], the Gibbs free energy of the missing sulfur-containing secondary phases $\text{La}_2\text{O}_2\text{S}$ ^[26], $\text{La}_2\text{O}_2\text{SO}_4$ ^[27] and $\text{La}_2(\text{SO}_4)_3$ ^[28] were added together with the SSUB5 database, which did not consider these phases in the database. With this, the final obtained LSCF + S database is able to perform thermodynamic simulations of the sulfur poisoning phenomena in LSCF cathode materials. More importantly, to make thermodynamic predictions, a fixed number of thermodynamic conditions are needed to obtain reliable results, which is based on the following concerns. Firstly, the simulation conditions should reflect the current experimental operating conditions as shown above, which include a temperature range from 800 up to 1,000 °C, a $P(\text{O}_2)$ range from Argon (10^{-5} atm) up to ambient atmosphere (0.21 atm) and a fixed 10 ppm $P(\text{SO}_2)$ based on the concentration of the actual gas we received from Airgas. Only in this way can the simulation results be comparable to our experimental observations. In addition, simulations should also mimic the general sintering and operation conditions under the actual or accelerating testing circumstances. Here, $P(\text{SO}_2)$, ranging from ppb level (~ 100 ppb in the atmosphere) to ppm level (accelerated testing condition), with $P(\text{O}_2)$, from ambient air on the surface down to the reducing conditions on TPBs due to the polarization effect^[29] is considered as the atmospheric conditions in the simulations. And the temperature is from 600 to 800 °C as the general operating temperature for IT-SOFCs (Intermediate-Solid Oxide Fuel Cells). Finally, the influence of the Sr content is considered in the current simulation to investigate the relationship between the Sr content and sulfur poisoning phenomenon, of which LSCF-8228, LSCF-7328 and LSCF-6428 are chosen. Finally, the sulfur poisoning results of the current LSCF cathode were cross-compared with the most widely-used LSM20 ($\text{La}_{0.8}\text{Sr}_{0.2}\text{MnO}_3$)^[17] cathode in our previous literature to better understand the sulfur-tolerant cathode in the future.

RESULTS AND DISCUSSIONS

The CALPHAD simulation approach introduced above was applied to the LSCF-6428 cathode in 10 ppm SO_2 conditions, shown in Figure 1 as a function of temperature, where Figure 1A is for dry air and Figure 1 is for Argon. It should be noted that the simulation is based on 0.1 mole molecule of the LSCF-6428 cathode. More importantly, the dry air condition is for the surface of the LSCF cathode (the cathode-gas interface), while the argon condition is for the TPBs (the cathode-electrolyte-gas interface) due to the polarization effect^[14]. It can be seen that the sulfur-containing phase, SrSO_4 , will be thermodynamically stable over the temperature range (600-1,000 °C) in both dry air and argon atmospheric conditions. However, at higher temperatures, the amount of SrSO_4 formed drops more severely in the argon condition than in dry air, indicating that the SrSO_4 secondary phase is more thermodynamically favorable in higher $P(\text{O}_2)$, which agrees well with the literature^[5,12] and suggests that the formation of the sulfates necessitates the oxidation of SO_2 . Furthermore, the stability of the sulfate phase decreases with increasing temperature in both dry air and Argon, suggesting that sulfate formation favors lower temperature conditions. In addition, a halite phase, instead of the spinel phase, shows up as the stable Co-Fe oxide phase at high temperatures in Argon [Figure 1B], but not in dry air, which is also intuitive due to the lower valance of the cations in reducing conditions. It is also worth mentioning that in both conditions, the structure of the spinel phase will change with increasing temperature from a Co-rich spinel (spinel #2) to a Fe-rich spinel (spinel #1) due to the miscibility gap of the spinel phase. The stability of two spinel structures is predicted thermodynamically but may be different from the actual experimental observations.

Results from the experimental characterization of LSCF-6428 samples heat-treated in both dry air and Argon were then cross-compared with the simulation results for empirical validation. The XRD spectra of the pre-sintered LSCF-6428 and the heat-treated samples are shown in Figure 2. It is apparent from the figure that some secondary phases do form during sulfur poisoning heat treatment experiments, which mainly correspond to the SrSO_4 phase. Meanwhile, a few isolated peaks cannot be identified due to their limited signals, which the simulations suggest could be related to the formation of other oxide phases. More

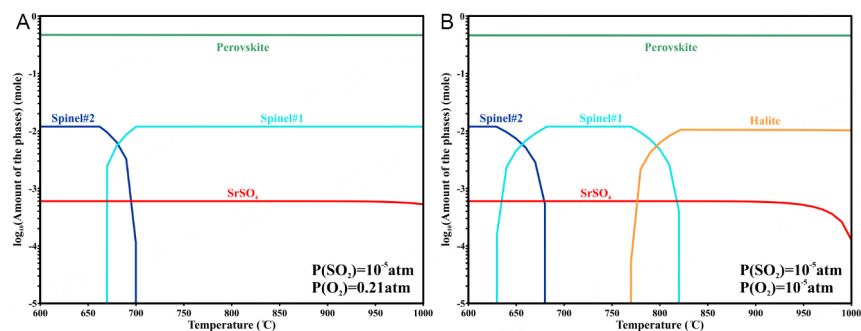


Figure 1. Computational results of the stability of LSCF-6428 under 10 ppm SO_2 in terms of temperature in a) dry air and b) argon.

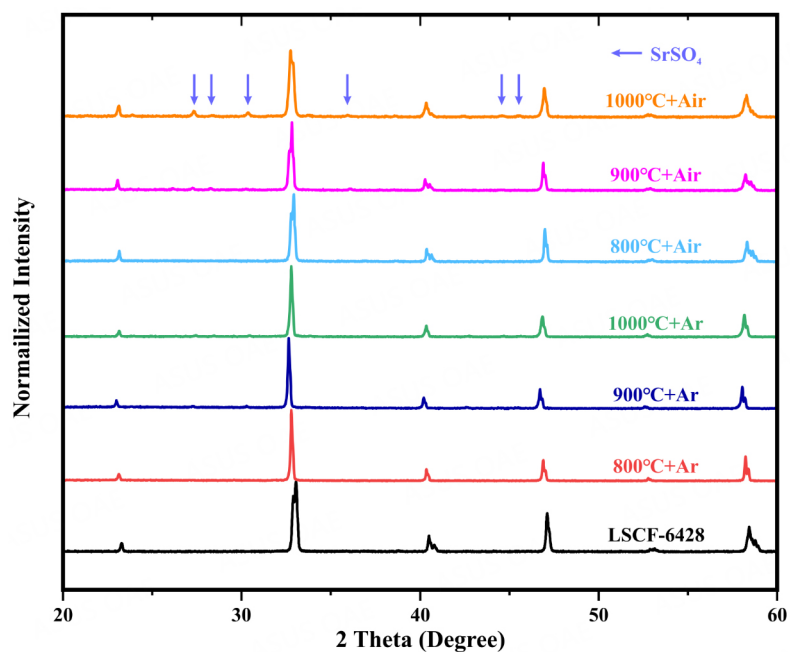


Figure 2. XRD spectra of the LSCF-6428 pellet (denoted as LSCF-6428) and heat-treated samples under the corresponding experimental conditions.

importantly, it can be seen from [Figure 2](#) that the peaks of the SrSO_4 phase are more pronounced in the dry air condition and at higher temperatures, indicating that the process for the formation of the SrSO_4 phase is governed both thermodynamically and kinetically, as its formation is thermodynamically favored at higher oxygen partial pressure and lower temperature conditions.

To further identify and verify the phases formed during the LSCF-6428 heat-treatment experiments, electron microscopy analysis was used to image and spectroscopically measure the spatial elemental distribution of the samples heat-treated in 10 ppm SO_2 containing atmosphere for 2 days, shown in [Figure 3](#), where [Figure 3A](#) is for dry air at 1,000 °C, [Figure 3B](#) is for dry air at 800 °C, and [Figure 3C](#) is for Argon at 1,000 °C, respectively. In 1,000 °C dry air [[Figure 3A](#)], there are two different grain morphologies besides the LSCF matrix based on the SEM-EDS mapping results: larger grains correspond to the Sr, S, and O-rich phases, while smaller ones are rich in Co, Fe, and O, which agrees well with the thermodynamic predictions from [Figure 1](#). Similarly, as shown in [Figure 3B](#), two different secondary phases were observed in the 800 °C dry air sample. The large but limited grains were a Co, Fe, and O-rich phase, while the tiny but well-

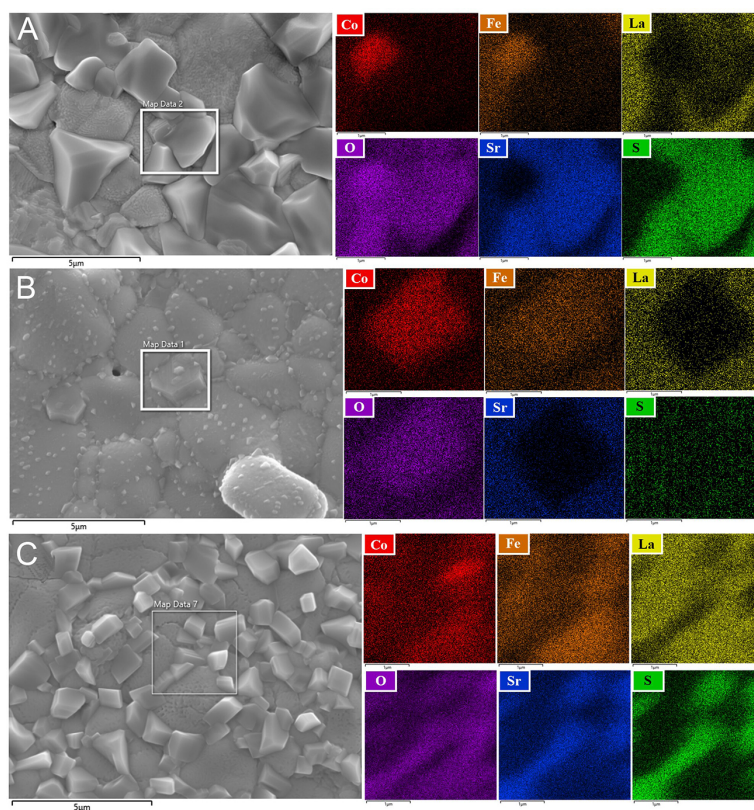


Figure 3. SEM micro-image and the corresponding EDS mapping results of the selected region of heat-treated LSCF-6428 for 2 days under 10 ppm SO₂ balanced with (A) dry air at 1,000 °C; (B) dry air at 800 °C, and (C) argon at 1,000 °C.

distributed grains along the larger grain boundaries and on the surfaces of the LSCF matrix cannot be characterized through SEM-EDS due to resolution/signal limitations. However, they were still believed to be the SrSO₄ phase based on the 1,000 °C dry air SEM-EDS and the predictions, where the SrSO₄ phase is thermodynamically more favorable at the lower temperature condition. The SEM results also indicate that the formation of the SrSO₄ is a kinetically limited process due to the apparent particle size difference (smaller SrSO₄ particles at a lower temperature), while the formation of the spinel phase is more likely governed by thermodynamics as there is no apparent grain size effect between the two temperature conditions. Finally, SEM-EDS results for the sample in Argon at 1,000 °C [Figure 3C] show that the average size of the SrSO₄ phase grained formed at 1,000 °C in Argon is between those formed under the conditions of 1,000 °C in dry air and 800 °C in dry air, indicating that the formation of the SrSO₄ phase is also governed by P(O₂) when kinetics are not constrained by lower temperature. In general, the SEM-EDS results support the predictions from our thermodynamic simulations regarding the formation of the secondary phases of the LSCF cathode under SO₂ poisoning conditions. However, further electron microscopy characterization at higher resolution is also needed to draw determining conclusions about the exact identity of the secondary phases formed, especially the crystal structure of the oxides present.

To characterize the nano-scale features on the surface of the LSCF samples, particularly the S-rich and Co-rich phases, TEM imaging, diffraction, and spectroscopic elemental mapping (STEM-EDS) were performed on lift-out samples prepared by focused ion beam (FIB), shown in Figures 4 and 5 for the sample treated at 800 °C in dry air (same sample as Figure 3B), and in Figures 6 and 7 for the sample treated at 1,000 °C in Argon (same sample as Figure 3C). The regions of interest (ROIs) in Figure 4 and Figure 6 were chosen for

Table 1. Quantification results from STEM-EDX analysis of LSCF treated at 800 °C in dry air from the ROIs in Figure 4

	ROI-4A (atomic %)	(% error)	ROI-4B (atomic %)	(% error)
O	58.01	0.17	60.30	0.03
S	0.04	13.72	0.05	13.49
Fe	3.91	0.11	17.25	0.12
Co	37.95	0.04	3.71	0.30
Sr	0.04	8.22	7.96	0.19
La	0.05	2.51	10.72	0.10

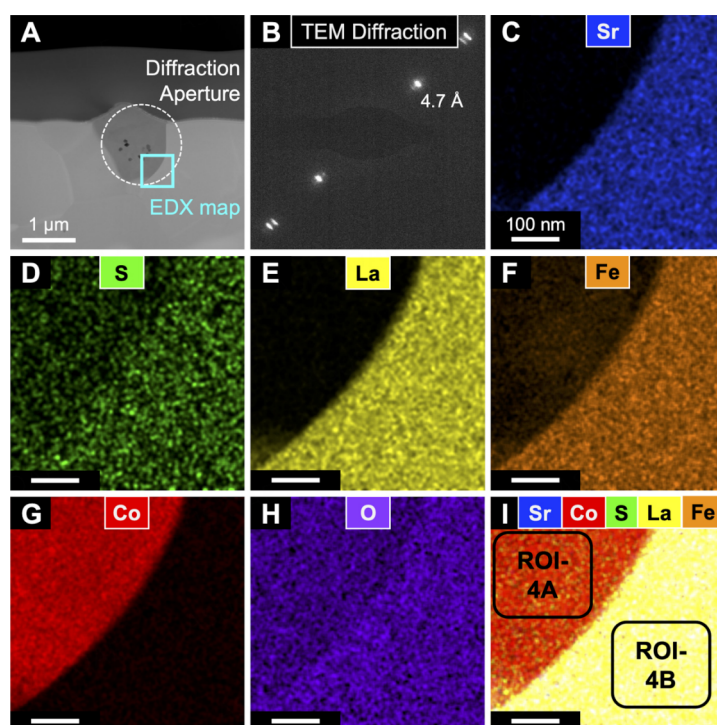


Figure 4. TEM characterization of a Co-rich region of the LSCF surface after treatment in dry air at 800 °C. (A) Dark field STEM image of Co-rich surface nanocrystal. White circle marks the location of the SAD aperture used to acquire a diffraction pattern of the nanocrystal, and the cyan box marks the location of the STEM EDS elemental map (C-I); (B) TEM diffraction pattern of nanocrystal; d-spacing values match those of Co_3O_4 for d_{111} ; (C-H) STEM-EDX elemental maps for Sr, S, La, Fe, Co, and O, displayed as relative atomic composition for each element; (I) combined elemental map for atomic fractions of Sr, S, La, Co, and Fe. ROI-4A and ROI-4B mark the regions where atomic composition was quantified using the STEM-EDS data, shown in Table 1.

containing large Co-rich phase crystals, and the ROIs in Figure 5 and Figure 7 were chosen for containing several tiny S-rich phase crystals. For LSCF at 800 °C in the air [Figure 4], the surface crystal (ROI-4A) only contains Cr and O (and trace Fe), at ca 3:4 ([Co/Fe]:O) atomic ratio by STEM-EDS analysis [Table 1]. Based on TEM diffraction of the same surface crystal [Figure 4B], the measured d-spacing values are consistent with Co_3O_4 , spinel #1, which fits the EDS composition results and agrees well with our modeling predictions. While the small surface crystal (ROI-5A) in Figure 5 only contains Sr, S, and O, at ca 1:1:2.5 atomic ratio by STEM-EDS analysis [Table 2]. Based on the TEM diffraction of the surface crystal, shown in Figure 5B, the crystal's measured d-spacing values are consistent with SrSO_4 . Based on the STEM-EDX and TEM diffraction analysis of the LSCF sample treated in dry air at 800 °C, it can be concluded that the Co/O rich phase is primarily composed of the spinel #1 phase ($[\text{Co/Fe}]_3\text{O}_4$), while the small S-rich surface grains are SrSO_4 , in agreement with the simulation predictions [Figure 1A].

Table 2. Quantification results from STEM-EDX analysis of LSCF treated at 800 °C in dry air from the ROIs in Figure 5

	ROI-5A (atomic %)	(% error)	ROI-5B (atomic %)	(% error)
O	50.31	1.49	46.14	0.34
S	22.98	1.15	0.04	10.15
Fe	0.88	7.58	23.17	0.05
Co	0.20	26.91	5.12	0.09
Sr	24.96	1.12	11.17	0.16
La	0.67	5.38	14.35	0.09

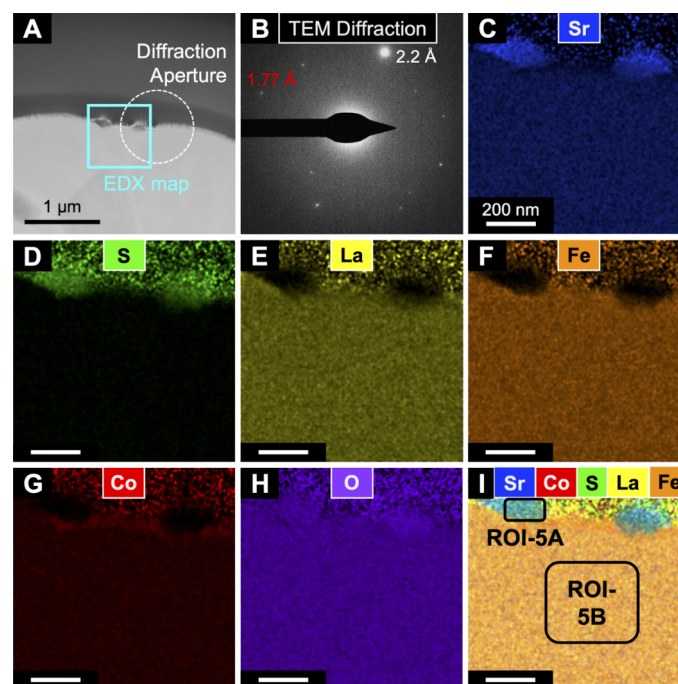


Figure 5. TEM characterization of a Sulfur-rich region of the LSCF surface after treatment in dry air at 800 °C. (A) Dark field STEM image of S-rich surface nanocrystals. White circle marks the location of the SAD aperture used to acquire a diffraction pattern of the nanocrystal, and the cyan box marks the location of the STEM EDS elemental map (C-I); (B) TEM diffraction pattern of nanocrystal; d-spacing values match those of SrSO_4 for d_{220} and d_{303} ; (C-H) STEM-EDX elemental maps for Sr, S, La, Fe, Co, and O, displayed as relative atomic composition for each element; (I) combined elemental map for atomic fractions of Sr, S, La, Co, and Fe. ROI-5A and ROI-5B mark the regions where atomic composition was quantified using the STEM-EDS data, shown in Table 2.

For the LSCF sample treated in Argon at 1,000 °C, the near-surface crystal (ROI-6A) in Figure 6 only contains Cr and O (and trace Fe), at ca 1:1 ([Co/Fe]:O) atomic ratio by STEM-EDS analysis [Table 3]. Based on TEM diffraction of the same crystal [Figure 6B], the measured d-spacing values are consistent with Co_1O_1 , halite, which agrees with our modeling predictions. The surface crystal (ROI-7B) in Figure 7 only contains Sr, S, and O, at ca 1:1:4 atomic ratio by STEM-EDS analysis [Table 3], and based on TEM diffraction of the surface crystal [Figure 7B], the crystal's measured d-spacing values are consistent with SrSO_4 . From experimental characterization using the STEM-EDX and TEM diffraction, it can be concluded that the LSCF sample treated in Argon at 1,000 °C has a Co/O rich phase that is primarily composed of the halite phase ($[\text{Co/Fe}]_1\text{O}_1$), while the small S-rich surface grains are SrSO_4 , also in agreement with our simulation predictions [Figure 1B].

Table 3. Quantification results from STEM-EDX analysis of LSCF treated at 1,000 °C in Argon from the ROIs in Figure 6

	ROI-6A (atomic %)	(% error)	ROI-6B (atomic %)	(% error)
O	51.36	3.28	60.31	1.71
S	0.12	0.02	0.02	0.00
Fe	0.27	0.04	17.35	1.93
Co	48.06	3.32	3.45	0.45
Sr	0.04	0.01	7.72	0.94
La	0.15	0.02	11.15	1.10

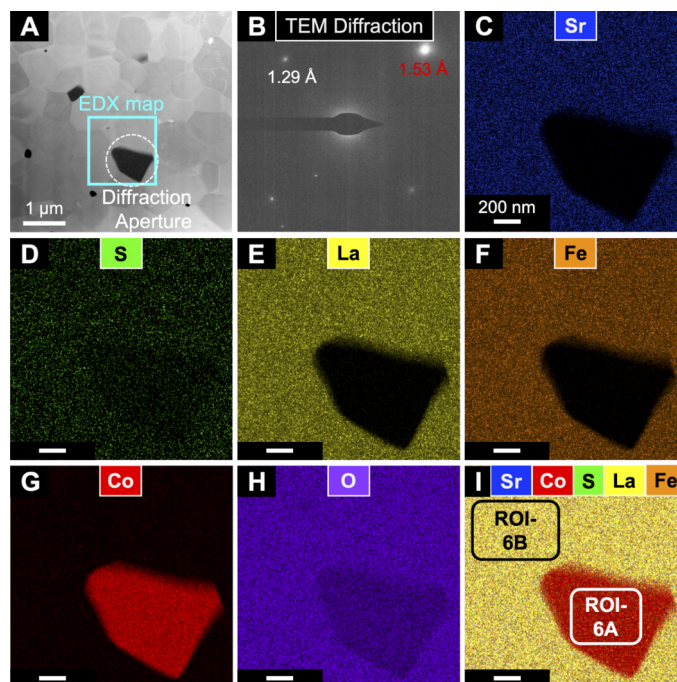


Figure 6. TEM characterization of a Co-rich region of the LSCF surface after treatment in Argon at 1,000 °C. (A) Dark field STEM image of Co-rich nanocrystal. White circle marks the location of the SAD aperture used to acquire a diffraction pattern of the nanocrystal, and the cyan box marks the location of the STEM EDS elemental map (C-I); (B) TEM diffraction pattern of nanocrystal; d-spacing values match those of Co_3O_4 for d_{022} and d_{133} ; (C-H) STEM-EDX elemental maps for Sr, S, La, Fe, Co, and O, displayed as relative atomic composition for each element; (I) combined elemental map for atomic fractions of Sr, S, La, Co, and Fe. ROI-6A and ROI-6B mark regions where atomic composition was quantified using the STEM-EDS data, shown in Table 3.

So far, the combined approach of CALPHAD simulation and XRD, SEM, and TEM characterization has provided a deeper insight into the sulfur poisoning phenomena of LSCF cathode material in the presence of SO_2 under various treatment temperatures and gas environments. Furthermore, the good agreement between the thermodynamic predictions and the experimental observations for LSCF highlights the utility of computational tools to study materials degradation phenomena in SOFC systems. Thus, further simulations were conducted to address more specific details, such as the influence of the LSCF cathode's Sr-composition on its sulfur poisoning, the validity of the SO_2 accelerated testing method for LSCF cathodes, and the long-term degradation mechanism(s) during the sulfur poisoning of LSCF cathodes.

Table 4. Quantification results from STEM-EDX analysis of LSCF treated at 1,000 °C in Argon from the ROIs in Figure 7

	ROI-7A (atomic %)	(% error)	ROI-7B (atomic %)	(% error)	ROI-7c (atomic %)	(% error)
O	59.57	0.29	66.28	0.21	51.14	0.43
S	0.04	12.67	16.13	0.10	0.11	18.78
Fe	19.88	0.08	0.18	2.97	3.91	0.61
Co	1.90	0.29	0.06	7.56	41.41	0.10
Sr	4.70	0.37	17.29	0.18	0.55	5.78
La	13.90	0.04	0.06	3.85	2.88	0.44

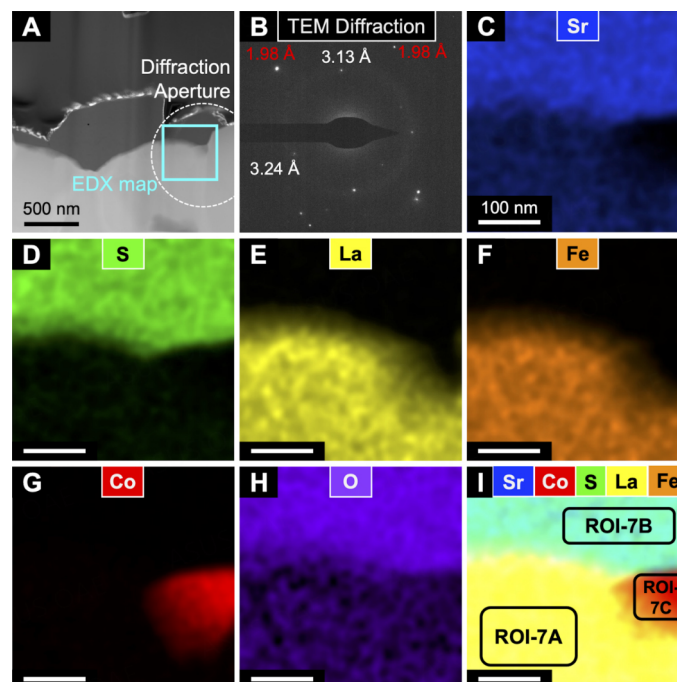


Figure 7. TEM characterization of a Sulfur-rich region of the LSCF surface after treatment in Argon at 1,000 °C. (A) Dark field STEM image of S-rich surface nanocrystals. White circle marks the location of the SAD aperture used to acquire a diffraction pattern of the nanocrystal, and the cyan box marks the location of the STEM EDS elemental map (C-I); (B) TEM diffraction pattern of nanocrystal; d-spacing values match those of SrSO_4 for d_{102} , d_{210} , and d_{401} ; (C-H) STEM-EDX elemental maps for Sr, S, La, Fe, Co, and O, displayed as relative atomic composition for each element; (I) combined elemental map for atomic fractions of Sr, S, La, Co, and Fe. ROI-7A, ROI-7B, and ROI-7C mark the regions where atomic composition was quantified using the STEM-EDS data, shown in Table 4.

To test the effect of Sr concentration on the sulfur poisoning phenomena of LSCF cathode materials, three commonly used compositions, LSCF-6428, LSCF-7328, and LSCF-8228, listed from highest to lowest Sr content, respectively, were chosen as candidates for investigation using simulations. The thresholds for the formation of SrSO_4 with these three candidates are plotted in Figure 8 as a function of $P(\text{SO}_2)$ and temperature, where Figure 8A is for treatment in dry air while Figure 8B is for treatment in Argon. The SrSO_4 stable region infers that the SrSO_4 phase is thermodynamically stable under given conditions, while the SrSO_4 free region suggests the chemical instability of the SrSO_4 phase. Consequently, the optimal operating condition for each composition would be in the SrSO_4 free region to prevent the formation of the detrimental SrSO_4 secondary phase. The threshold diagrams show that the SrSO_4 phase is thermodynamically more favorable at lower temperatures, higher $P(\text{SO}_2)$, higher $P(\text{O}_2)$, and for higher Sr composition electrodes. This agrees well with our experimental observations for LSCF-6428, shown in Figure 3. It also matches well with prior studies by Wang *et al.*^[7,11], where the formation of SrSO_4 was

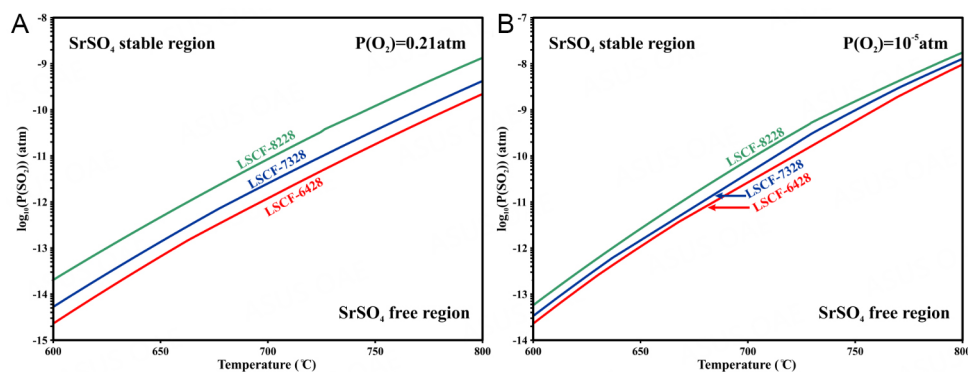


Figure 8. SrSO₄ threshold diagrams in terms of the P(SO₂) and temperatures for LSCF-6428 (red), LSCF-7328 (blue) and LSCF-8228 (green) under (A) dry air and (B) Argon.

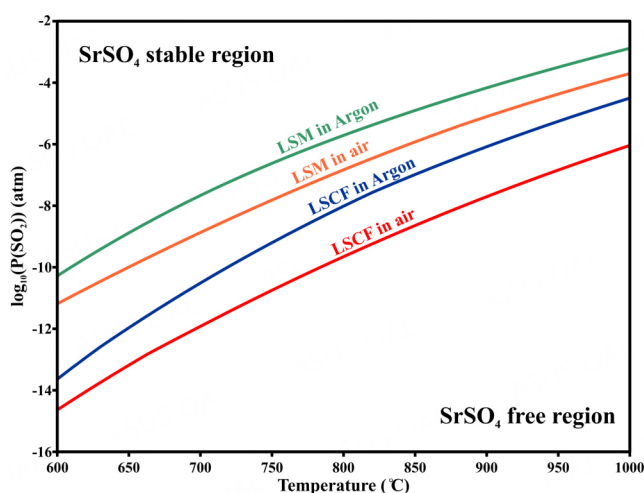


Figure 9. SrSO₄ threshold diagrams in terms of the P(SO₂) and temperatures LSCF-6428 and LSM20 under air and argon conditions.

observed in the presence of 1, 10, and 100 ppm SO₂ but not in 0.1 ppm SO₂, and where sulfur poisoning was more pronounced at lower temperatures. In addition, Wang *et al.*^[9] investigated the effect of Sr concentration on the sulfur poisoning of LSCF by mainly using LSCF-6428 and LSCF-8228. Their results showed that the thickness of SrSO₄ formed in LSCF-6428 was almost four times thicker than that in LSCF-8228, which has the lower relative Sr composition of the two LSCF materials.

Under typical P(SO₂) atmospheric conditions, the only sulfur-containing secondary phase observed to form in LSCF cathodes is SrSO₄^[6-12,30,31]. It is widely accepted that the formation of SrSO₄ is responsible for the long-term degradation of the LSCF cathode materials^[5]. Based on the simulation results in Figure 8, the threshold for SrSO₄ formation in LSCF-6428 at 800 °C is around 10⁻¹⁰ atm in air and 10⁻⁸ atm under reducing conditions. The typical (SO₂) content in the ambient air is at the level of 10⁻⁷ atm, indicating that ambient SO₂ in the air is sufficient to drive long-term degradation of the LSCF-6428 cathode. Therefore, sulfur poisoning results from accelerated testing, which is done at elevated SO₂ levels, should mimic the natural sulfur poisoning that occurs during cathode operation at standard testing conditions with atmospheric SO₂, as in both cases, there is excess SO₂. Thus, accelerated testing will not only reduce the total time for running poisoning experiments but is also capable of reproducing the sulfur poisoning phenomena that occur in the presence of ambient SO₂ during standard testing conditions. In systems where the CALPHAD simulations

predict that ambient SO_2 will be insufficient to drive SrSO_4 stability, the use of accelerated testing can potentially generate erroneous experimental results regarding SrSO_4 poisoning related to standard testing conditions^[17]. Using this simulation approach, the reliability of accelerated testing can be scrutinized for different cathode materials under different environmental conditions.

The threshold diagrams of the LSCF cathode suggest that LSCF has poor sulfur tolerance under operating conditions, and finding an alternative sulfur-resistant cathode material thus remains of great importance. To better understand the sulfur poisoning of LSCF cathode in the context of other potential cathode materials, CALPHAD threshold diagrams were created for LSM20^[17] and compared to LSCF-6428 in terms of $P(\text{SO}_2)$ and temperature under air and argon atmospheric conditions, as shown in Figure 9. Simulations predict that LSM20 has superior sulfur resistance to LSCF-6428 both in the air and argon conditions. Specifically, the threshold of SrSO_4 stability for LSM20 is around 10^{-7} atm at 800 °C in air, while it is 10^{-10} atm for LSCF-6428. Unlike LSCF-6428, LSM20 could be free from sulfur poisoning at ambient SO_2 . This sulfur resistance behavior was also experimentally observed by Liu *et al.*^[6], where LSM20 was found to be free from sulfur poisoning even following exposure to 1ppm of SO_2 for 1,000 h, and the degradation rate at 20 ppm SO_2 for LSCF-6428 was 8 times higher than that of LSM20. These computational and experimental results confirmed that the LSCF cathode is a poor sulfur-tolerant material in comparison with LSM. One potential solution for the poor sulfur resistance of LSCF is to place an additional sulfur filter before contacting the LSCF cathode to purge the sulfur concentration to below the threshold concentration. Another solution would be to utilize a core-shell structure^[32], having LSM as the sulfur-protecting shell and LSCF cathode as the core.

CONCLUSIONS

In this work, we have evaluated the sulfur poisoning behavior of LSCF cathode materials in the presence of SO_2 with a combined computational and experimental approach and tested the reliability of the simulation method for predicting sulfur poisoning behavior under different environmental conditions. The results from CALPHAD simulations regarding the stability of the secondary phases were validated using the experimental characterization, XRD, SEM, and TEM, of the same cathode materials following operations at the simulation conditions. Further simulation predictions were made to better understand the effects that other determining factors, such as temperature, $P(\text{O}_2)$, $P(\text{SO}_2)$, and cathode Sr-composition, have on the formation of SrSO_4 and the overall sulfur poisoning behavior. We find that the formation of SrSO_4 on LSCF cathodes (sulfur poisoning) is more thermodynamically favorable at lower temperatures, higher $P(\text{SO}_2)$, higher $P(\text{O}_2)$, and higher Sr composition. Finally, comparisons were made between LSCF-6428 and LSM20 cathode materials, which confirmed that LSCF-6428 has a much lower sulfur tolerance than LSM20, in agreement with recent literature. The CALPHAD simulation approach used here can be extended to other potential cathode systems to theoretically test their tolerance to poisoning at different environmental conditions, which has the potential to accelerate the experimental development of novel poisoning-resistant cathode materials.

DECLARATIONS

Authors' Contributions

Made substantial contributions to conception and design of this research, data analysis, writing the draft and editing: Wang R

Performed data analysis, figures preparation, writing-review and editing: Parent LR

Made substantial contributions to conception and design of this research, data analysis, funding acquisition, writing and editing: Zhong Y

Availability of data and materials

Not Applicable.

Financial support and sponsorship

This material is based upon work supported by the Department of Energy under Award Number (DE-FE0031652). The authors would like to thank the support and guidance from the DOE National Energy Technology Laboratory program managers, Jason Montgomery, Venkat Venkataraman and Andrew O'Connell.

Conflicts of interest

All authors declared that there are no conflicts of interest.

Ethical approval and consent to participate

Not applicable.

Consent for publication

Not applicable.

Copyright

© The Author(s) 2023.

REFERENCES

1. Skinner SJ. Recent advances in Perovskite-type materials for solid oxide fuel cell cathodes. *Int J Inorg Mater* 2001;3:113-21. DOI
2. Stambouli A, Traversa E. Solid oxide fuel cells (SOFCs): a review of an environmentally clean and efficient source of energy. *Renew Sustain Energy Rev* 2002;6:433-55. DOI
3. Schuler AJ, Wuillemin Z, Hessler-wyser A, Van Herle J. Sulfur as pollutant species on the cathode side of a SOFC system. *ECS Trans* 2009;25:2845-52. DOI
4. Xiong Y, Yamaji K, Horita T, et al. Sulfur poisoning of SOFC cathodes. *J Electrochem Soc* 2009;156:B588-92. DOI
5. Wang F, Kishimoto H, Ishiyama T, et al. A review of sulfur poisoning of solid oxide fuel cell cathode materials for solid oxide fuel cells. *J Power Sources* 2020;478:228763. DOI
6. Liu RR, Taniguchi S, Shiratori Y, Ito K, Sasaki K. Influence of SO₂ on the long-term durability of SOFC cathodes. *ECS Trans* 2011;35:2255-60. DOI
7. Wang F, Yamaji K, Cho D, et al. Sulfur poisoning on La_{0.6}Sr_{0.4}Co_{0.2}Fe_{0.8}O₃ cathode for SOFCs. *J Electrochem Soc* 2011;158:B1391-7. DOI
8. Wang DJ, Jing L. Effect of SO₂ on performance of solid oxide fuel cell cathodes. Available from: <https://www.semanticscholar.org/paper/Effect-of-SO2-on-Performance-of-Solid-Oxide-Fuel-De-jun-Jing/82c3339827f4bedfe62b0270ecab17a1aac3d0ca#citing-papers> [Last accessed on 9 Mar 2023].
9. Wang F, Yamaji K, Cho D, et al. Effect of strontium concentration on sulfur poisoning of LSCF cathodes. *Solid State Ionics* 2012;225:157-60. DOI
10. Wang F, Yamaji K, Cho D, et al. Evaluation of sulfur dioxide poisoning for LSCF cathodes. *Fuel Cells* 2013;13:520-5. DOI
11. Wang C, Jiang SP. Mechanism of SO₂ poisoning on the electrochemical activity of LSCF and LSM electrodes. *ECS Trans* 2015;68:1023-9. DOI
12. Wang F, Kishimoto H, Develos-bagarinao K, Yamaji K, Horita T, Yokokawa H. Interrelation between sulfur poisoning and performance degradation of LSCF cathode for SOFCs. *J Electrochem Soc* 2016;163:F899-904. DOI
13. Darvish S, Asadikiya M, Hu B, Singh P, Zhong Y. Thermodynamic prediction of the effect of CO₂ to the stability of (La_{0.8}Sr_{0.2})_{0.98}MnO_{3±δ} system. *Int J Hydrogen Energy* 2016;41:10239-48. DOI
14. Darvish S, Gopalan S, Zhong Y. Thermodynamic stability maps for the La_{0.6}Sr_{0.4}Co_{0.2}Fe_{0.8}O_{3±δ}-CO₂-O₂ system for application in solid oxide fuel cells. *J Power Sources* 2016;336:351-9. DOI
15. Darvish S, Wang CC, Jiang SP, Zhong Y. Thermodynamic stability mapping and electrochemical study of La_{1-x}Sr_xCo_{0.2}Fe_{0.8}O_{3±δ} (x = 0.2-0.4) as a cathode of solid oxide fuel cells in the presence of SO₂. *Electrochim Acta* 2018;287:68-77. DOI
16. Darvish S, Hu B, Singh P, Zhong Y. Thermodynamic and experimental evaluation of La_{1-x}Sr_xMnO_{3±δ} cathode in presence of Cr-containing humidified air. *JOM* 2019;71:3814-24. DOI
17. Wang R, Parent LR, Gopalan S, Zhong Y. Experimental and computational investigations on the SO₂ poisoning of (La_{0.8}Sr_{0.2})_{0.95}MnO₃ cathode materials. *Adv Powder Mater* 2023;2:100062. DOI

18. Walker E, Ammal SC, Suthirakun S, Chen F, Terejanu GA, Heyden A. Mechanism of sulfur poisoning of $\text{Sr}_2\text{Fe}_{1.5}\text{Mo}_{0.5}\text{O}_{6-\delta}$ perovskite anode under solid oxide fuel cell conditions. *J Phys Chem C* 2014;118:23545-52. DOI
19. Su M, Huan D, Hu X, Zhu K, Peng R, Xia C. Understanding the favorable CO_2 tolerance of Ca-doped LaFeO_3 perovskite cathode for solid oxide fuel cells. *J Power Sources* 2022;521:230907. DOI
20. Ta N, Chen M, Zhang L, et al. Numerical simulation of kinetic demixing and decomposition in a $\text{LaCoO}_{3-\delta}$ oxygen membrane under an oxygen potential gradient. *J Membr Sci* 2018;548:526-39. DOI
21. Wang CC, Darvish S, Chen K, et al. Combined Cr and S poisoning of $\text{La}_{0.8}\text{Sr}_{0.2}\text{MnO}_{3-\delta}$ (LSM) cathode of solid oxide fuel cells. *Electrochim Acta* 2019;312:202-12. DOI
22. Xu H, Cheng K, Chen M, Zhang L, Brodersen K, Du Y. Interdiffusion between gadolinia doped ceria and yttria stabilized zirconia in solid oxide fuel cells: experimental investigation and kinetic modeling. *J Power Sources* 2019;441:227152. DOI
23. Sabarou H, Wang R, Zhong Y. The origin of the phase separation in $(\text{La}_{0.8}\text{Sr}_{0.2})_{0.95}(\text{Cr}_x\text{Fe}_{1-x})\text{O}_{3\pm\delta}$ perovskites for oxygen transport membranes applications. *Solid State Ion* 2020;349:115293. DOI
24. Cheng K, Xu H, Zhang L, et al. Computational engineering of the oxygen electrode-electrolyte interface in solid oxide fuel cells. *NPJ Comput Mater* 2021;7:119. DOI
25. Zhang W, Barfod R. Investigation of degradation mechanisms of LSCF based SOFC cathodes-by CALPHAD modeling and experiments. Available from: <https://orbit.dtu.dk/en/publications/investigation-of-degradation-mechanisms-of-lscf-based-sofc-cathod> [Last accessed on 9 Mar 2023].
26. Kumar RV, Kay DAR. Thermodynamics of the Ca-S-O, Mg-S-O, and La-S-O systems at high temperatures. *Metall Trans B* 1985;16B:287-94. DOI
27. Dwivedi RK, Kay DAR. Thermodynamics of the oxidation of rare earth oxysulfides at high temperatures. *Metall Trans B* 1984;15B:523-8. DOI
28. Kellogg HH. A critical review of sulfation equilibria. Available from: https://archive.org/details/sim_american-institute-of-mining-metallurgical-petroleum_1964-12_230_7/page/n131/mode/2up [Last accessed on 9 Mar 2023].
29. Levy C, Zhong Y, Morel C, Marlin S. Thermodynamic stabilities of $\text{La}_2\text{Zr}_2\text{O}_7$ and SrZrO_3 in SOFC and their relationship with LSM synthesis processes. *J Electrochem Soc* 2010;157:B1597-601. DOI
30. Gao J, Li L, Yin Z, Zhang J, Lu S, Tan X. Poisoning effect of SO_2 on the oxygen permeation behavior of $\text{La}_{0.6}\text{Sr}_{0.4}\text{Co}_{0.2}\text{Fe}_{0.8}\text{O}_{3-\delta}$ perovskite hollow fiber membranes. *J Membr Sci* 2014;455:341-8. DOI
31. Liu RR, Wang DJ, Jing L. Effect of SO_2 on the performance of LSCF cathode. *Adv Mater Res* 2014;902:41-4. DOI
32. Gopalan S, Levitas B. Core-shell heterostructures as functional materials for solid oxide fuel cell (SOFC) electrodes. Available from: <https://www.osti.gov/biblio/1872369/> [Last accessed on 9 Mar 2023].